Predicting compressive stress-strain behavior of elasto-plastic porous media via morphology-informed neural networks

Lindqwister, W.; Peloquin, J.; Dalton, L. E.; Gall, K.; Veveakis, M.

DOI
10.1038/s44172-025-00410-9

Publication date
2025

Document Version
Final published version

Published in
Communications Engineering

communications engineering

A Nature Portfolio journal

Article

https://doi.org/10.1038/s44172-025-00410-9

Predicting compressive stress-strain behavior of elasto-plastic porous media via morphology-informed neural networks

W. Lindqwister [1,2,4] ✉, J. Peloquin [3,4] ✉, L. E. Dalton [1], K. Gall[3] & M. Veveakis[1]

Porous media, ranging from bones to concrete and from batteries to architected lattices, pose difficult challenges in fully harnessing for engineering applications due to their complex and variable structures. Accurate and rapid assessment of their mechanical behavior is both challenging and essential, and traditional methods such as destructive testing and finite element analysis can be costly, computationally demanding, and time consuming. Machine learning (ML) offers a promising alternative for predicting mechanical behavior by leveraging data-driven correlations. However, with such structural complexity and diverse morphology among porous media, the question becomes how to effectively characterize these materials to provide robust feature spaces for ML that are descriptive, succinct, and easily interpreted. Here, we developed an automated methodology to determine porous material strength. This method uses scalar morphological descriptors, known as Minkowski functionals, to describe the porous space. From there, we conduct uniaxial compression experiments for generating material stress-strain curves, and then train an ML model to predict the curves using said morphological descriptors. This framework seeks to expedite the analysis and prediction of stress-strain behavior in porous materials and lay the groundwork for future models that can predict mechanical behaviors beyond compression.

Porous materials exist in abundance throughout nature, many with unique morphologies that define their shape and function. These morphologies range from having highly ordered structures, such as a honeycomb created by a colony of bees, to disordered or stochastic structures such as the random frequency and distribution of pores in volcanic rock. Whether investigating ordered or disordered structures, the meso-scale mechanical properties of these materials have been found to be intrinsically linked to their structure at the micro-scale[1]. In the geomaterial space, porous materials like rocks have found processes like strain localization[2–4], fault reactivation[5–7], and granular flow[8] largely dependent on microstructural morphology[9,10]. Engineered porous materials, such as ceramics[11] and energy storage materials[12], have found similar conclusions. In the field of biomaterials, the interplay between the microstructural morphology, osseointegration, and mechanics of bone[13] have highlighted the importance of understanding the effects of structural morphology for porous materials.

For studying the intricate morphology of porous materials, methods like X-ray computed tomography (CT) have exponentially increased the resolution of imaging and enabled digital 3D reconstructions. However, the memory size of these datasets make high-throughput finite element analysis (FEA) simulation costly and impractical in certain applications[14,15]. To address this bottleneck, extensive research has been conducted in extracting morphological features from porous materials to characterize these structures for mathematical analysis. Recently, a combination of multiple tools such as skeletonization and Patch Interface Shape Detection was introduced to extract information about the topology, patch interface lengths, and patch interface shapes of the microstructure[16]. Using this approach, the authors were able to choose a robust microstructure representation with salient features. Selection of features is critical in capturing the necessary information about a microstructural morphology. Nadiri et al.[17] chose a different set of features with morphology characterizations made using sphericity, signifying irregularity, and projected area. The process of manually extracting features from microstructural data is tedious, and for large datasets it becomes less practical. Automated workflows and programs have been created that can extract features such as grain area, slenderness ratio, globular volume fraction, and colony size, with minimal user input[18–20]. Due to the already extensive research and availability of morphological feature

[1]Department of Civil and Environmental Engineering, Duke University, Durham, USA. [2]Technische Universiteit Delft, Delft, Netherlands. [3]Department of Mechanical Engineering and Materials Science, Duke University, Durham, USA. [4]These authors contributed equally: W. Lindqwister, J. Peloquin.
✉e-mail: wlindqwister@tudelft.nl; jake.peloquin@duke.edu

extraction methods, this work focused on utilizing these methods to characterize porous material microstructures and create descriptive features that are well-suited for machine learning (ML) implementation and predictive of mechanical behavior.

For the particular case of porous materials, Minkowski functionals were selected as the primary geometric morphometers M_i, with the idea emerging from the fields of statistical and digital rock physics[21], where Minkowski functionals were used to describe phenomenon such as the spin of galaxies[22] to the permeability of porous media[23]. The use of these functionals as the linkage between microstructural geometry and meso-scale phenomenon is supported by Hadwiger's theorem[24], which states that $d+1$ Minkowski functionals can effectively characterize the geometric shape and composition of a microstructure, with d representing the dimension of the geometric system. All other descriptors that are additive, motion-invariant and conditionally continuous are a linear combination of the above functionals. In the case of a 3D system, the four Minkowski functionals of the domain formed by the grains of the microstructure Ω are the total volume of grains

$$M_0(\Omega) = \int_{\Omega} dV, \tag{1}$$

the total grain surface area

$$M_1(\Omega) = \int_{\partial\Omega} dS, \tag{2}$$

their total mean curvature, with r_1 and r_2 representing the principal radii of curvature of the surface element dS

$$M_2(\Omega) = \int_{\partial\Omega} (1/r_1 + 1/r_2) dS, \tag{3}$$

and their total Gaussian curvature, which directly relates to the Euler characteristic χ via the Gauss-Bonnet theorem[21]

$$M_3(\Omega) = \int_{\partial\Omega} (1/r_1 r_2) dS = 4\pi\chi(\Omega). \tag{4}$$

Through Biot's seminal work on understanding porous material grain-scale features, it has been shown that a porous material's microstructural geometry directly correlates with meso-scale properties such as strength[1,25]. When referring to a porous or composite structure, the mechanical properties of the structure are often referred to as "effective" properties, such as effective elastic modulus, to clarify their distinction from a sample of the given material with zero porosity. With these descriptors readily extractable from voxelized images of 3D microstructures, it stands to reason that these Minkowski functionals would be invaluable in predicting a porous material's mechanical behavior through an ML framework[26,27].

Indeed, the development of ML algorithms for training on FEA simulation data has enabled the discovery of relationships that previously may have been too time-consuming to gather data for or too complicated in general, such as predicting the stress-strain curve of a material[28,29] or determining optimal composite designs for maximizing crack resistance[30–32]. For understanding the mechanical behavior of a material, a stress-strain curve provides an invaluable amount of information about its strength, deformation, and rigidity. Thus, in this work we selected the elastic region and the onset of the plastic region from uniaxial compressive stress-strain curves to be the target data for training the ML model, with the intent to further develop the model to predict multiple loading stress-strain response curves in the future.

The overall goal of this research was to develop a systematic methodology for characterizing porous materials using scalar morphological descriptors and ML techniques to predict their response to compressive loading. As a starting point, uniaxial compressive behavior was investigated due to its ubiquity in real-world scenarios. By integrating physical and computational elasto-plastic experiments with advanced morphometric analysis and ML, we aim to expedite the calculation of structure-property relationships in porous materials across a variety of fields including geomaterials, structural biomaterials, and energy storage materials. This approach seeks to present a step toward overcoming the challenges associated with the complexity and variability of porous media microstructures, enabling faster predictions of mechanical behavior. ML models trained on morphological features offer great potential for applications such as accelerating multiscale simulations, enabling real-time structural health monitoring, and optimizing additive manufacturing processes in-situ.

Methods

Selected dataset

The dataset was curated from microstructural CT scans gathered using a variety of resources. The online database digitalrocksportal.org[33] provided many publicly available 3D CT scans of various materials. All data sourcing can be found in Supplementary Table 2. These scans consisted of material samples ranging from rock to wood to coral, binarized and cropped as voxelized stacks of images. In total, the original dataset consisted of 161 raw samples. Due to the high resolution of these scans (at a minimum, $750 \times 750 \times 750$ voxels, with many double the size), the raw samples were segmented into sub-samples, multiplicatively increasing the size of the available dataset to 4200. Ultimately, 654 sub-samples were used for FEA simulation and training of the ML model. It is important to note that this sub-sampling technique created sub-samples that, although not being identical, were extracted from the same raw material sample. This has been accounted for in the selection of the ML training and evaluation sets.

Representative elementary volume analysis

One area of consideration when segmenting 3D images for ML data set generation is to find a representative elementary volume (REV), so that the selected sub-samples are representative of the raw material sample. REV analysis consists of analyzing properties of interest for randomly selected sub-samples to understand how the segmented volume of a particular sub-sample affects its calculated morphological properties. As the size of the sampling volume increases, the values of individual properties should converge to those of the raw sample[34].

Due to the variable nature of the raw data used in this scientific study (differing resolutions, CT scanning parameters, raw sample sizes, etc), REV analysis was performed to normalize volumes for training such that all sub-samples were composed of identical voxel counts, and to determine the minimum sub-sampling volume for cropping the 3D microstructures. To address this issue of dataset scaling, all Minkowski functionals must be normalized to be scale-invariant[35]. Due to Euler characteristic and surface area being inherently dependent on the tortuosity and resolution of a microstructure, respectively, both of these values are directly correlated with the volume of a sample. However, literature has shown that normalizing these values via sample volume tends to yield acceptable REV results[34–36]. Furthermore, the correlation coefficient of a scatter plot of non-normalized Euler numbers versus varied volumes gives an indicator on the scale-invariance of a microstructure, with a higher correlation coefficient corresponding to a more scale-invariant microstructure[36].

As seen in Fig. 1, REV analysis for porosity, surface area, and Euler characteristic visibly converged to scale-invariant values. The minimum sampling volume fraction that, for all three REV scales, achieved variance less than the threshold value of 0.01 was 0.2 voxels/voxels. This indicates that microstructural properties remain scale-invariant up to a volume fraction 0.2, giving a lower bound to the sub-sampling method described in methods and Fig. 2. With a minimum raw sample volume of $750 \times 750 \times 750$ voxels, a sub-sampling cube size of $150 \times 150 \times 150$ voxels was selected.

Morphometer extraction pipeline

To extract geometric morphometers from the voxelized 3D microstructures, the open source digital reconstruction and image processing software

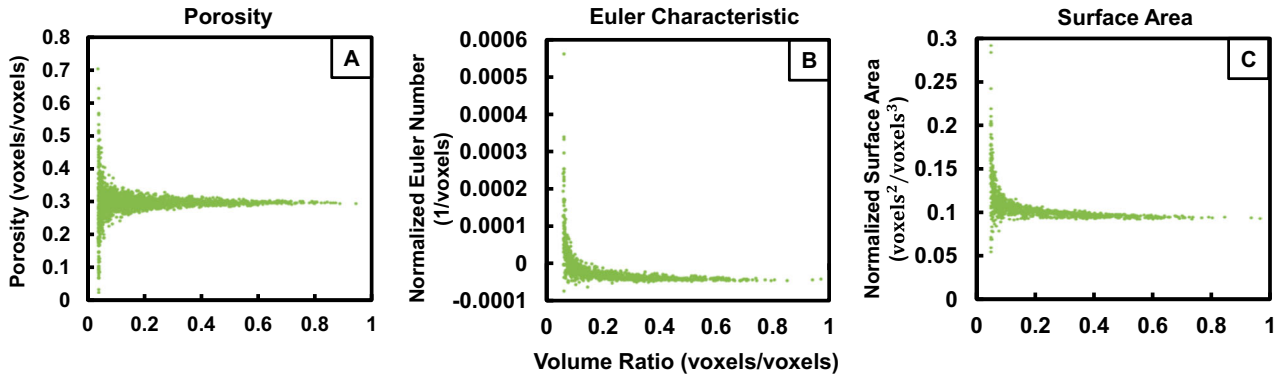

Fig. 1 | Results from representative elementary volume (REV) analysis. A Porosity values assessed from randomly sampled volumes. **B** Surface area values, normalized by volume, assessed from randomly sampled volumes. **C** Euler characteristic values, normalized by volume, assessed from randomly sampled volumes.

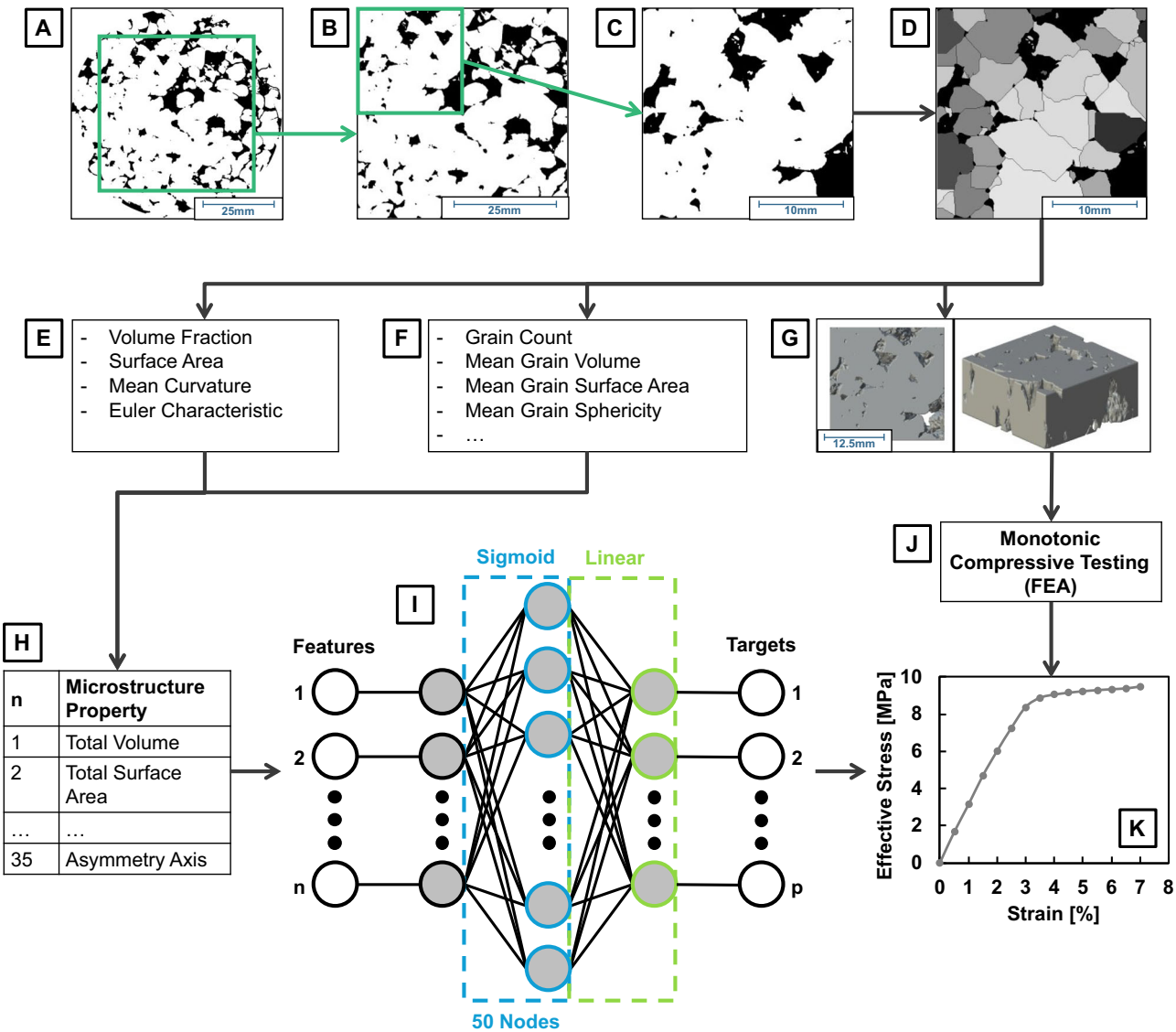

Fig. 2 | Graphical representation of ImageJ morphometer extraction workflow and machine learning (ML) process. A Original scan of raw sample. **B** Cropped original scan to create rectangular prism. **C** Subscan of cropped scan. **D** Subscan with individual grains identified via Watershed algorithm. **E** Minkowski functionals and (**F**) mean grain morphological descriptors are calculated and exported as .CSV file. **G** A 3D surface mesh file of the entire subscan microstructure is exported as STL file. **H** Minkowski functionals and mean grain descriptors are combined for each sub-sample and used to (**I**) train a neural network. The mesh files are used to (**J**) perform monotonic compression testing via finite element analysis (FEA), and (**K**) the stress-strain curves are then given to the network as targets for training. The number of inputs are represented by n and the number of outputs are represented by p, where n are morphological features of the microstructure and p are stress values for points along the elastic and into the plastic region of the stress-strain curve for the respective microstructure.

ImageJ and the morphometer extraction library MorpholibJ[37] were used. This process is represented schematically in Fig. 2 and is briefly described here: Upon importing and cropping the voxelized 3D image to a rectangular prism, the image was automatically binarized to separate the solid and void portions. This cropped prism was then segmented into smaller prisms to increase the dataset size for ML. A marker-based watershed segmentation algorithm was then performed on the subscan to separate and label each of the solid grains within the material[38]. With the image segmented and the individual grains identified, morphological analysis was completed using the MorphoLibJ plugin. M_0, the total volume of grains, was calculated by counting the total number of voxels in the 3D image and converting this value to porosity by dividing by the total bounding size of the image. Surface area, M_1, was calculated following Lang et al., and is described in the MorpholibJ manual[37]. Per Armstrong et al. and Guevel et al., total mean curvature M_2 is captured by the mean grain size[10,21], which is quantified as the mean breadth in MorpholibJ. The mean breadth $\bar{b}$ of a convex set is the average of the caliper diameter over all directions, and for a domain Ω with a smooth boundary $\partial\Omega$, is proportional to the integral of the mean curvature[37,39] as follows:

$$\bar{b} = \frac{1}{2\pi}\int_{\partial\Omega}\frac{\kappa_1(x)+\kappa_2(x)}{2}dS \tag{5}$$

with $\kappa_{1,2}(x)$ representing the principal curvatures of a surface. These quantities are inversely related to the radii of curvature identified in Eq. (3). The final morphometer M_3, Gaussian curvature, is quantified through the Euler characteristic indicated in Eq. (4), where the Euler number in 3D is calculated through 6-connectivity. As with M_0, $M_{1,2,3}$ were all normalized by image volume to ensure feature scalability.

Outside of the four normalized Minkowski functionals, 31 other microstructural features were extracted for ML model training to verify the feature significance of the Minkowski functionals and see which combinations of features resulted in the highest model performance. As indicated in Supplementary Table 3, these additional features included angular orientation values for describing the anisotropy of the structure, number of voxels within the structure, and more[37]. The additional 31 features were also examined to quantify potential anisotropy of the materials. Hadwiger's theorem assumes a motion-invariant—or isotropic—microstructure[24], meaning the microstructural measurements are expected not to vary heavily in any direction, which is reflected in the scalar representation of Minkowski functionals. Although porous materials tend to be largely isotropic, it was hypothesized that the sub-sampling method may have increased the effects of local anisotropy potentially making additional features a requirement for accurate ML predictions.

Finite element analysis

With a sufficient dataset of 3D microstructures and their extracted morphometers, FEA simulations with an elasto-plastic constitutive law were performed to generate a compressive stress-strain curve for each sub-sample. The open-source, parallel-processing capable finite element package MOOSE/REDBACK was used as the main FEA platform[40,41]. Through a python-based scripting pipeline, MOOSE/REDBACK was fed voxelized microstructural volumes for high-throughput analysis, with meshing performed through its built-in microstructure mesh generator. Following the methodology of Lesueur et al. (2017)[42], these subscan volumes were imported into MOOSE as image stacks of .tif files, creating voxel-based hexahedron elements corresponding to the individual voxels of the image stack. To speed up the collection of FEA simulation data, a mesh convergence study was performed to potentially reduce the order of nodes on the mesh and to exponentially decrease simulation time. From the mesh convergence study, a minimum mesh of $50 \times 50 \times 50$ nodes was found to invoke just a 5% error on the final converged value. Thus, the mesh was coarsened down to $50 \times 50 \times 50$ nodes from $150 \times 150 \times 150$, decreasing individual simulation time from 30 hours to 1 hour at a relatively minimal cost to simulation accuracy.

The focus of this work was to predict compressive stress-strain behavior using the Minkowski functionals, and particular emphasis was not placed on a specific material application as the authors believe the developed methodology could, in similar form, apply to many different porous materials. However, to further explore the predictive capabilities of the trained model with application to real-world loading scenarios, the material parameters for FEA were chosen to correspond with those of a readily available 3D printable material. In the absence of the physical material samples used for generating the raw CT dataset, selection of this 3D printable material enabled fabrication of physical representations of the CT dataset that could be physically tested and compared with the FEA results.

The FEA was set up to simulate uniaxial compression. Thus, each mesh was subject to fixed displacement rate loading across the top face of the cube while the bottom of the sub-sample remained fixed. Each sub-sample was scaled to a size of 22 mm x 22 mm x 22 mm and loaded at a rate of 5 mm/min. A Young's modulus of 2.6 GPa and Poisson ratio of 0.35 were used to simulate the material behavior of the 3D printing material selected: Formlabs Grey Pro resin. Properties for this material were determined as per ASTM D695 using the same printer, material, and testing apparatus as described in the methods section. Beyond the standard material properties, a non-linear plasticity tensor following the Von Mises J2 plasticity criterion was implemented alongside an isotropic elasticity tensor to simulate both linear and nonlinear behavior of the material[43]. An isotropic, constant strain hardening was implemented, integrating the behavior into the material without bogging down high-throughput calculations for relatively limited accuracy gains.

Microstructure-informed neural networks

The extracted morphometers and FEA results were used for training an ML model to predict uniaxial compressive stress-strain curves from the morphometers. The morphometers (see Supplemental Table 3) were used as input features, providing morphological information about the microstructure. Model training was conducted separately with the entire set of 35 extracted morphometers as input, and then with only the four Minkowski functionals as input for performance comparison against the entire set of morphometers. The targets during model training were the compressive stress-strain curves calculated using FEA, which consisted of 250 pairs of stress and strain data points for each microstructure. To reduce the target dimensionality, all curves were sampled at 15 equally spaced strain values before being used for model training, resulting in 15 stress values for the targets of each sample.

The ML algorithm used to train the model was selected to be a neural network. A wide variety of approaches have been studied for using neural networks to predict the mechanical behavior of materials based on structural characteristics[28–30,44–48], and the network designs used in these studies motivated the design of the neural network used in this work. Specifically, Hassanin et al. showed that accurate predictions of strictly periodic porous lattice mechanical properties could be made from a relatively small amount of training data and features using a simple network consisting of three hidden layers each with 50 nodes[45].

Using these network parameters as a starting point, a multi-dimensional search grid of parameter combinations was developed to fine-tune the network parameters for the given dataset. As shown in Table 1, three network parameters were varied during the grid search optimization: nodes per layer, number of hidden layers, and activation function. With ten options of nodes per layer, between one and five hidden layers, and four activation functions, creating all possible combinations resulted in a total of 200 unique parameter combinations for the grid search. For each parameter combination, 10-fold cross validation was performed with a training-validation ratio of 80:20. With 600 samples used for model training, this resulted in 480 training set samples and 120 validation set samples in each fold. Each model was pre-trained using an unsupervised greedy layer-wise technique[45] and the training method used was Levenberg-Marquardt (a damped least squares method with interpolation between the Gauss-Newton algorithm and gradient descent) with mean square error (MSE) as

Table 1 | Table containing the neural network parameters used to create a grid search during model training

Nodes per Layer	Number of Hidden Layers	Activation Function
15	1	Linear
30	2	ReLU
45	3	SiLU "Swish"
60	4	Sigmoid
75	5	-
90	-	-
105	-	-
120	-	-
135	-	-
150	-	-

The grid search was performed using each unique combination of parameters above, resulting in 200 unique combinations from ten node per layer values, five hidden layer numbers, and four activation functions. After network training using each unique combination of parameters, each trained network had performance evaluated using a reserved set of test samples unused during model training.

the objective function to be minimized. Network training was stopped when any of the following stopping criteria were met:

- At least 1000 training epochs occurred.
- The performance gradient fell below 1e-07.
- The adaptation parameter (mu) rose above 1e10.
- Validation error increased more than 6 times since the last time it decreased.

After training, the performance of each model was further evaluated using the set of 54 randomly selected evaluation samples that were withheld from the training process. It should noted, however, that the training/evaluation set split was made such that no sub-samples within the evaluation set were extracted from the same raw sample as any sub-sample in the training set. This ensured that the evaluation set sub-samples were truly dissimilar from those used in model training. Ultimately, a network consisting of one hidden layer with 50 nodes and a sequential set of Sigmoid to Linear activation functions were selected based on model performance during the grid search and the relative simplicity of the model compared to similarly performing models with more layers or nodes (within an R^2 of ± 0.001) (Fig. 2).

Physical sample fabrication and testing

As FEA results were collected, experimental tests were performed to verify the FEA results with physical analogues. A Formlabs Form2 stereolithography (SLA) printer was used with Formlabs Grey Pro resin and a layer height of 0.05 mm to fabricate the physical samples. This method of 3D printing was selected because it is fast, it produces parts less anisotropic in nature than traditional fused deposition modeling (FDM) printing, and it is considerably less expensive than powder-based printing methods. After printing, uniaxial compression testing was performed on the 3D printed microstructures using a Test Resources 830E5 testing apparatus, as shown in Fig. 3. The compression testing was performed at a load rate of 5 mm/min until an end strain value of 50% was reached (for 22 mm height samples this resulted in a strain rate of $0.004\ s^{-1}$). The experimentally collected compressive stress-strain curves were compared to those calculated with the FEA simulation. In total, 20 unique sub-samples from 20 different raw samples were fabricated and physically tested, with $N = 3$ duplicates of each sub-sample to account for variance.

Results

Automated workflow efficiency

The speed at which the automated workflow collects data was determined by dividing the workflow into five steps: 1) segmenting the CT scan and extracting geometric morphometers, 2) applying a finite element mesh and running the FEA, 3) concatenating FEA results with morphometers to create a database for ML, 4) performing the hyper-parameter optimization grid search, and 5) training the final model. The average per-sample time was computed for relevant steps, and the results were tabulated in Supplementary Table 1. Once the raw sample file had been stored in the proper directory location, the process was completed automatically and requires no user input.

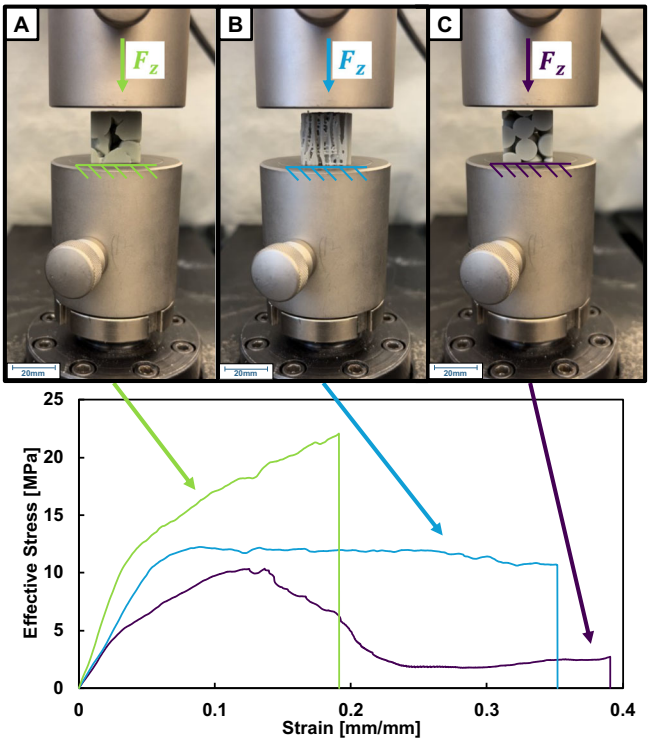

Fig. 3 | Experimental loading of a 3D printed microstructure sample in compression, using a Test Resources 830E4 testing machine. Scans used are (**A**) Scan032-053, (**B**) Scan013-092, and (**C**) Scan007-102.

Machine learning results and performance

Using the complete set of 35 input features and 15 target output stress values, the model performed well with a training R-square value of 0.969 and an evaluation set R-square value of 0.943 (Fig. 4). There were a few notable samples that had predictions with considerably less accuracy than others, represented by the strands deviating farthest from the parity line. After achieving success using the complete set of 35 input features, the model was retrained with only the four Minkowski functionals as input features. Based on Hadwiger's Theorem, as discussed in the introduction, it was hypothesized that these four functionals would accurately capture the microstructure geometry and thus provide the model with necessary information to create accurate predictions. After training the model with this reduced input feature space, an evaluation set R-square value of 0.939 was obtained (Fig. 4), showing a reduction in performance of only 0.004 from the original model trained with all 35 features.

To evaluate the effectiveness of Minkowski functionals as input features, model performance was compared across different feature sets. Figure 5 shows the evaluation set R^2 values for models trained with all 15 possible combinations of Minkowski functionals, all 35 extracted morphometric features, and only the 31 non-Minkowski morphometers. The M_0 (volume) and M_1 (surface area) functionals had a greater impact on improving stress-strain prediction accuracy compared to M_2 and M_3, which represent mean and Gaussian curvature, respectively. Although the highest performance was achieved using all 35 extracted morphometric features, as shown in Fig. 4, the model trained with just the four Minkowski functionals performed nearly as well. Models trained with only the 31 non-Minkowski morphometers showed similar performance

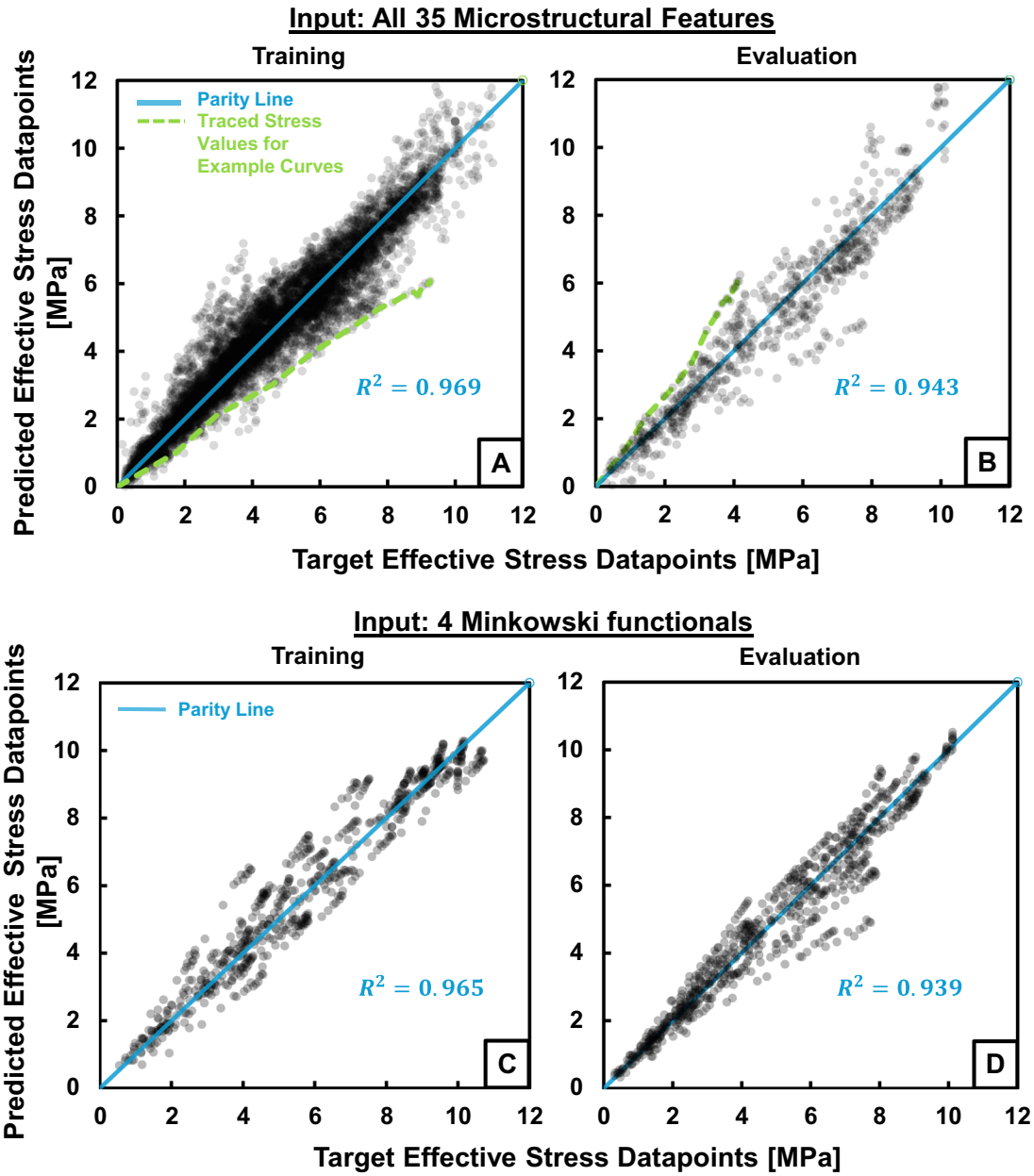

Fig. 4 | Coefficient of determination (R^2) plots for evaluating model performance. **A** Training set performance for predicted stress points on the curves. **B** Evaluation set performance for predicted stress points on the curves. The X and Y axes represent the error of the samples of the targets (X) to the predictions (Y). The green dashed lines are examples of connecting all target vs. prediction stress values for a single stress/strain curve. Thus, the distance between a green dashed line and the parity line represents the error between target and predicted stress values for that curve. The model was initially trained with all 35 microstructural features, and then (**C**) retrained and (**D**) evaluated using only the 4 Minkowski functionals.

to those using M_0 or M_1 alone. These performance patterns and potential explanations for the differences between feature sets are expanded on in the discussion section.

Although R-square provides a valuable metric for evaluating model performance, predicting elasto-plastic compressive stress-strain curves for the microstructures required further analysis to ensure realistic curves were being predicted. A custom MATLAB script was created to loop through all microstructures in the evaluation set and display a plot of the predicted vs. simulated compressive stress-strain curves. The plots were then sorted by average residual value of the 15 data points. Figure 6 displays four of these plots, three being pulled from the center of the distribution of plots and one being pulled from the lowest-performing samples. The plots showed that qualitatively, on average, the model predicted logical and accurate curves when compared to the FEA results. Predicted vs. simulated compressive stress-strain curves for all 54 evaluation set samples can be found in the supplementary material in Supplementary Data File 1 as the first 54 lines of the datafile.

Experimental validation of FEA

Experimentally gathered data was compared to scaled FEA results such that the size of the FEA cube matched the size of the 3D printed cube (22 mm × 22 mm × 22 mm). For each of the 20 physical sub-samples, the average Young's modulus and yield strength were calculated and compared to the FEA results. Across all 20 sub-samples, the mean percent error (MPE) between physical experiment and FEA for Young's modulus and yield strength was 4.8% and 7.4%, respectively, with the physical experiment taken as ground truth. Two randomly selected physical versus FEA comparisons are shown in Fig. 6, where we see a close matching between the

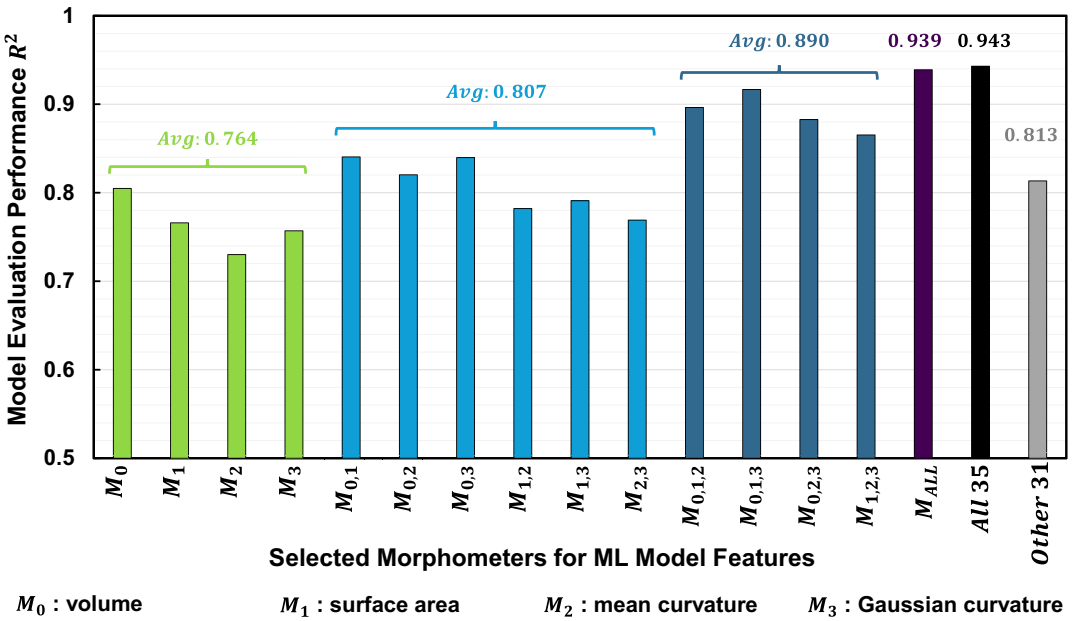

Fig. 5 | Coefficient of determination (R^2) results for evaluation set machine learning (ML) predictions using various combinations of morphological features as input. The model achieved the highest accuracy when utilizing all 35 extracted morphometric features, with comparable results obtained using only the four Minkowski functionals. Among these functionals, the M_0 (volume) and M_1 (surface area) descriptors had a greater influence on model performance than M_2 (mean curvature) and M_3 (Gaussian curvature).

experimentally gathered and numerically calculated results. The implications of these results for comparing experimental to simulation data through scaling are discussed in the discussion section below.

Discussion

The results of this scientific study and methodology development demonstrate not only the capabilities of Minkowski functionals as fast and accurate predictors of porous elasto-plastic material compressive behavior, but also that this is an effective framework for preparing 3D microstructures for high-throughput analysis.

The automated process of microstructure feature extraction is capable of producing data from CT scans at a highly efficient rate, nearly 2.2 seconds per sub-sample. Additionally, training the ML model took an insignificant amount of time compared to the FEA and experimental testing, effectively creating a "bottleneck" at this step. One possibility for reducing FEA simulation time would be to utilize high performance computing and run multiple simulations in parallel using a computing cluster. This would effectively both reduce the time per simulation and increase the amount of simulations run at one time. Utilization of high performance computing would be especially important for potential future studies where more complicated analysis that incorporates phenomenon beyond elasto-plastic behavior is included, such as damage, fracture, and internal contact, or where multiple loading modes are being simulated.

In Fig. 7A, the benefit of utilizing ML for these stress-strain curve predictions is highlighted for certain scenarios. In general, the number of samples required for training depends on desired model performance for the evaluation set and future predictions. For example, in this study, a training set size of approximately 450 samples would be required to achieve a model performance of $R^2 = 0.90$, while utilization of the entire available 600 training samples achieved a performance of 0.939 (using only Minkowski functionals as features in both cases). However, future prediction of stress-strain curves from materials dissimilar to those used in this study may require a greater training set size. Figure 7B indicates, based on the time requirements for FEA curve generation and model training documented in Supplementary Table 1, when it becomes favorable to utilize this predictive ML model over solely relying on FEA. Notably, for a given training set size, the ML model becomes less time-consuming when approximately equal or more stress-strain curve predictions are desired. Another key advantage of this method is the reduction of input feature space, which minimizes model complexity compared to conventional 3D neural networks. Despite the small dataset size of 654 sub-samples, the predictive power of the Minkowski functionals is evident, showcasing the method's effectiveness in linking microstructural descriptors to mechanical behavior.

The approach taken in this study is particularly appealing for scenarios requiring numerous predictions for porous materials with morphologies similar to those in the training set. For example, in multiscale analyses like FE2 methods, lower-scale simulations could be substituted with this or a comparable ML model, enabling faster calculations while accounting for morphological changes at smaller scales through the use of Minkowski functionals. In real-time structural health monitoring, such a model could quickly predict stress-strain behavior based on sensor-detected morphological changes, allowing for faster response to potential issues in critical structures. Similarly, in additive manufacturing (AM), the model could be employed to monitor morphological variations during the build process and adjust parameters in real-time to ensure that the final product meets mechanical performance criteria, thus preventing defects and enhancing quality.

The results of the representative elementary volume (REV) analysis, shown in Fig. 1, indicate that the sub-samples of microstructures used are scalable and representative. Due to the relatively accurate ML predictions by the model and the voxel-size normalization detailed in our methods section, it is shown that 1) the sample scaling did not negatively affect the predictive capabilities of this model and 2) that a sufficient normalization scheme was used to address varying sizes and resolutions for individual samples.

While the REV analysis demonstrates the scale invariance of morphological descriptors, the issue of mechanical scaling, particularly in nonlinear, heterogeneous materials, presents a more nuanced challenge. Although Fig. 1 provides evidence of morphological invariance, mechanical responses do not always follow these trends, especially for materials with complex strain behaviors that are not as easily modeled using basic elasto-plastic methods. Size effects, such as strain localization emerging with increasing slenderness of the samples, could be potentially affecting the accuracy of the model's predictions at larger scales. While the model performs well for small sub-samples and 3D printed analogues, caution should

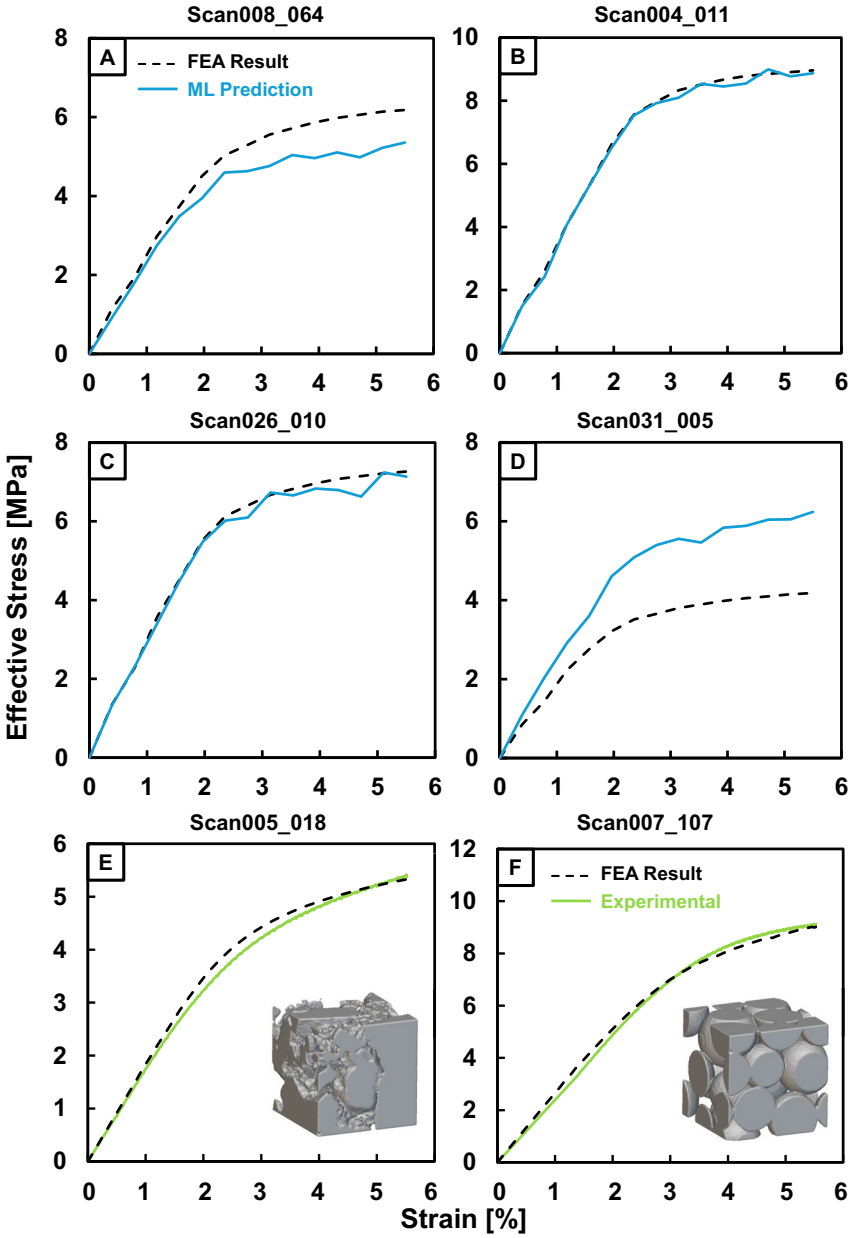

Fig. 6 | Compressive stress-strain curves from finite element analysis (FEA), machine learning (ML) predictions, and experimental tests for six randomly selected samples. A distribution of average residuals was generated for all predicted curves. (**A**) Scan008-064, (**B**) Scan004-011, and (**C**) Scan026-010 were randomly chosen from the middle 20 percent of the residual distribution, illustrating the typical accuracy of the model's predictions. **D** Scan031-005 represents a sample from the lowest-performing 25 percent, highlighting cases where the model struggled. **E**, **F** Comparisons between experimental compression tests and FEA results, along with digital representations of the corresponding porous samples.

be exercised when scaling predictions to larger structures without further validation, as mechanical behaviors at larger scales may deviate from the predictions made at smaller scales.

The performance of the ML model using only the four Minkowski functionals as input features underscores the power of these geometric descriptors. As demonstrated in Figs. 4 and 5, the reduction in performance was minimal when compared to models using all 35 extracted morphometric features. This supports Hadwiger's Theorem, which claims that these functionals are sufficient for capturing the essential geometry of the microstructure. Additional features could enhance model accuracy by capturing material anisotropy, but the Minkowski functionals alone provide an efficient and accurate method for describing the behavior of porous materials. Furthermore, the experimental validation of these results, shown in Fig. 8, highlights that materials with similar Minkowski functional values exhibit similar mechanical performance, even across different geological material types.

While the overall predictive power of the models remained strong, there were still some notable predictive outliers. This can likely be attributed to two key factors: mesh realization for certain microstructure subsections and data clustering on randomized train-evaluation splits. Figure 9 presents three examples of microstructure sub-samples with poor predictability in the current neural network framework, with Fig. 9A demonstrating a limitation of the current sub-sampling technique where some sub-samples of less-porous microstructures lead to samples that are effectively solid. Samples like these fall outside of the domain of analysis for our predictive method, and would naturally not perform well in the current predictive framework. With regards to the meshing technique, while a mesh convergence study was implemented to examine the largest acceptable degree of coarsening for a finite element mesh in order to increase simulation speed, this mesh convergence study was not performed on every data point. As such, some microstructures with very fine features in their meshes (such as solid structures that are just one or two voxels in size across) would likely be over-coarsened, leading to discrepancies in predicted stress-strain behavior vs simulated stress-strain behavior. Figure 9B is an example of this phenomenon, as this subscan has fine and floating details such as thin vertical columns and complex, fine-grain geometry that is not captured sufficiently on a coarsened mesh. Samples with many fine features like these are highly likely to have their compressive stress-strain behavior poorly reflected through the current simulation pipeline, leading to some inaccurate

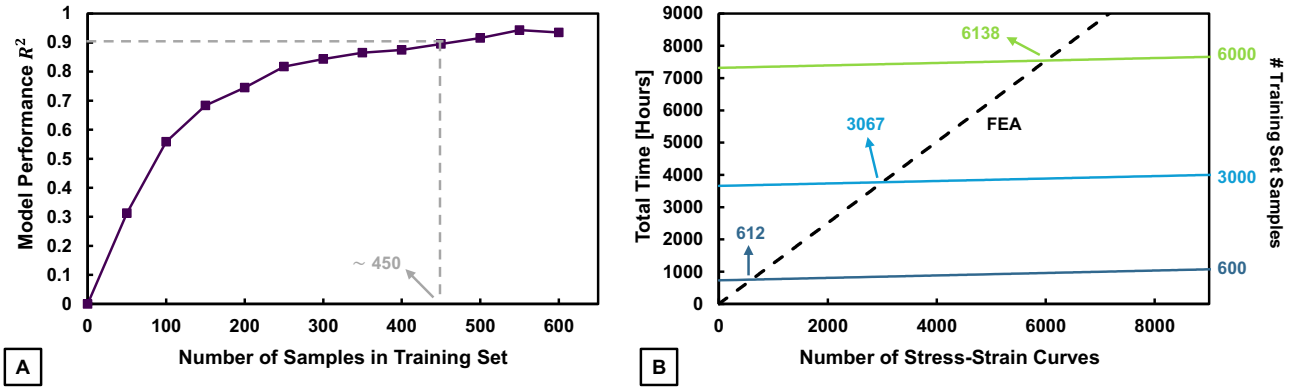

Fig. 7 | Effects of number of training set samples on both machine learning (ML) model performance and total combined time for model setup and prediction. **A** Plot of ML model coefficient of determination (R^2) versus size of the training dataset. The evaluation set was held constant, and model training was performed with increasing number of samples from the original training dataset to highlight improvement in model performance. For an evaluation set R^2 of 0.90, approximately 450 samples were required. **B** Plot of total analysis time versus number of desired stress-strain curve predictions from data tabulated in SI Table 1. Using finite element analysis (FEA), there is a linear relationship between time and number of curves produced through simulation, with no initial time cost. For ML models, there is an initial time cost for gathering training data and training the model. The dotted line shows the total analysis time to achieve a certain number of stress-strain curve predictions using FEA. It can be seen that, for example training set sizes of 600, 3000, and 6000 samples, using ML is less time intensive than FEA when more than 612, 3067, and 6138 different material sample stress-strain curve predictions are desired, respectively.

Fig. 8 | Experimental validation of correspondence between Minkowski functionals and compressive stress-strain behavior, specifically Young's modulus and yield strength. Subplots (**A**–**C**) display representative stress-strain curves from experimental testing of subscan pairs 1, 2, and 3, respectively. Images of the printed sample pairs prior to testing can be seen in the upper-right corner. The dash-outlined rectangle shows the linear-elastic and onset of plastic region from where the average and standard deviation of Young's modulus and yield strength were calculated and then plotted in subplots (**D**, **E**), respectively. The standard deviation was calculated using five duplicate experiments for each sample.

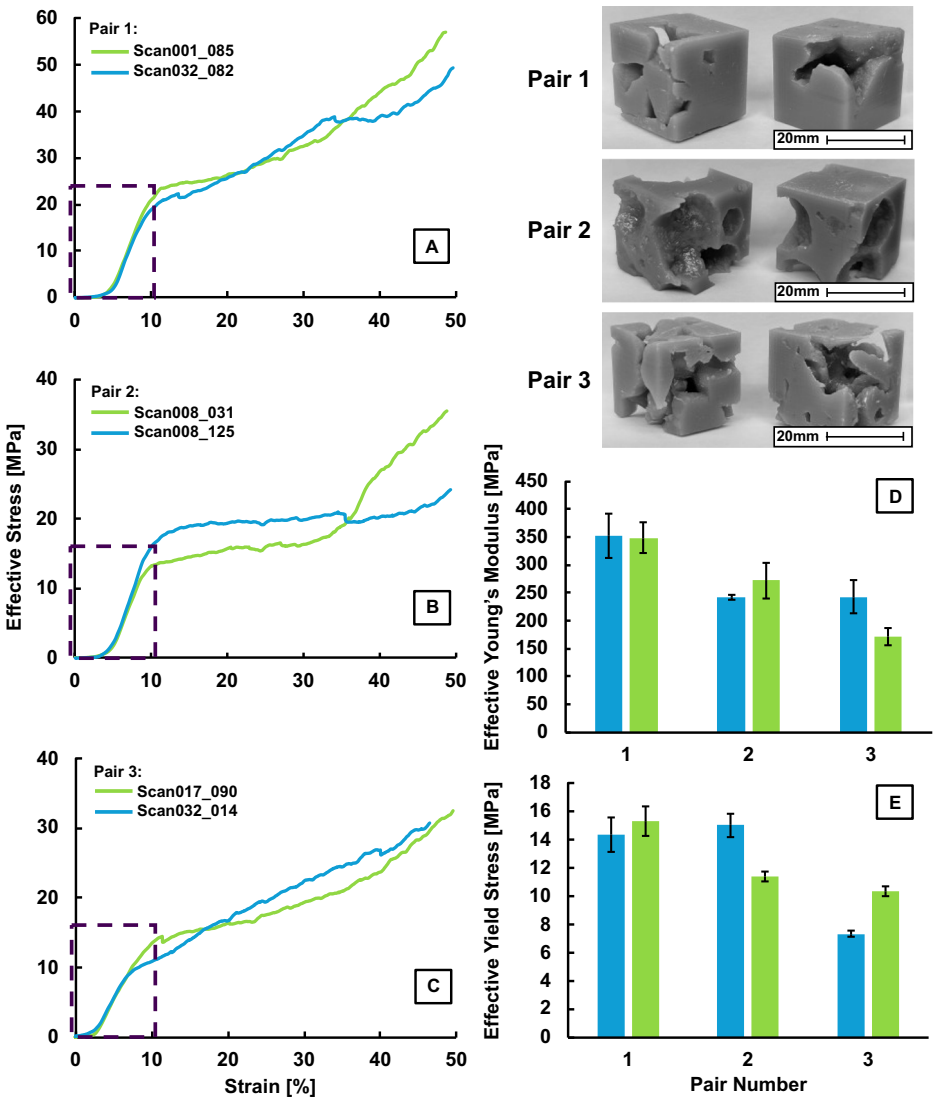

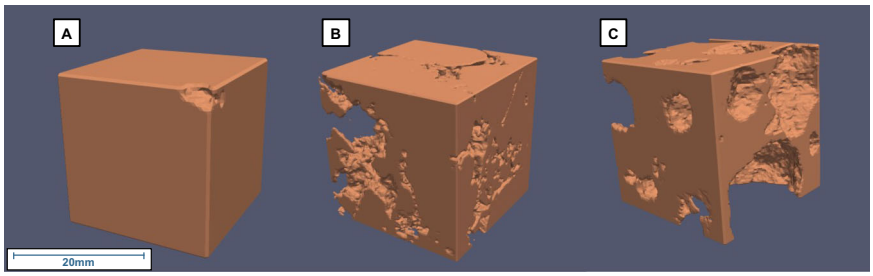

Fig. 9 | Example scans with aberrant results relative to the neural network's predictive output. **A** A subscan with almost no porosity/porous characteristics. **B** A subscan with floating and thin elements that are obscured by over-coarsened meshes. **C** A subscan with high internal concavity, which is more susceptible to failure modes outside of the simulation domain.

predictions. However, re-meshing these samples did improve the accuracy of some samples, but not to a noticeable degree where it would substantially upgrade overall model performance.

Another important factor where meshes appeared to be influencing the accuracy of FEA results came in cases with highly convex samples. Highly convex samples—essentially, samples with large contiguous void spaces with relatively low surface areas and Euler numbers close to zero—behaved more as hollow bodies than as blocks under compression. This meant that the solid scaffolding of these samples connecting the top boundary to the bottom boundary was relatively thin, leading to a solid that would be more likely to undergo buckling as opposed to squash-like compression. Figure 9C demonstrates a sample with highly convex internal geometry. This represents an important limitation of the finite element model used, where buckling moment behavior isn't explicitly accounted for in the simulation, and a material that fails in buckling may not be accurately represented in the elasto-plastic model utilized.

The relationship between R-square values and stress-strain curves, as shown in Fig. 4, also reveals that larger deviations from the predicted values are tied to specific mechanical features of the microstructures, particularly in the plastic region. This highlights the need for further refinement of the ML model to better capture non-linear behavior under varying stress conditions.

Conclusion

This study has demonstrated the effectiveness of using Minkowski functionals as key geometric descriptors to predict the mechanical behavior of porous elasto-plastic materials under uniaxial compressive loading. By integrating high-throughput morphological feature extraction, finite element analysis (FEA), and machine learning (ML), we developed a robust framework capable of accurately predicting compressive stress-strain responses. The strong performance of the ML model, particularly when trained on only four Minkowski functionals, underscores the power of these descriptors in capturing essential microstructural details. While the model has shown promise in accurately predicting behavior at simple uniaxial conditions at smaller scales, challenges remain in applying it to larger structures and more elaborate loading conditions due to factors that are not incorporated in the physics of the present approach, like potential change in the physics of the larger scale that would impose size effects and render the REV analysis of Fig. 1 non-representative of the structure, and dependency of the failure mode to the loading conditions in strain localization and fracture that would induce additional softening and non-uniqueness in the correlation of the microstructure with the stress-strain response. The limitations of the current meshing techniques and FEA methods for handling complex geometries and non-linear mechanical behavior also contribute to predictive outliers. Nonetheless, this work paves the way for broader applications, including multiscale analyses such as FE2 simulations, structural health monitoring, and additive manufacturing, where ML models could substitute lower-scale simulations for faster, real-time predictions. Future efforts will focus on refining the model for more complex mechanical behaviors, improving mesh handling, and extending the methodology to address anisotropic and heterogeneous materials.

Data availability

Additional data analysis plots, tables, and figures are available within the supplementary materials. The finite element, segmented scan, and network model that support the findings of this study are available through the Mendeley Data repository "Neural network architecture and training data for prediction of porous material mechanical properties based on their microstructure" (https://data.mendeley.com/datasets/9wpm748fb3/4)[49]. Base scan data used in this study can be traced from Supplementary Table 2. Furthermore, the FEA result data used to generate SI Figs. 1 and 2 is included as SI Data File 1. Additionally, the ML input and output data can be found in SI Data File 2.

Code availability

All code used in this study is available online on open access repositories. The segmentation code is available on GitHub via the repository "SegmentJ" (https://github.com/wlindqwister/SegmentJ). FEA input files are available on the Mendeley Data repository "Neural network architecture and training data for prediction of porous material mechanical properties based on their microstructure" (https://data.mendeley.com/datasets/9wpm748fb3/4)[49] in the folder "MOOSE Input Files". All input files are designed for use with the public release of the MOOSE finite element software along with the MOOSE app REDBACK, specifically the branch "18_macrodissipation." Finally, the machine learning model used in this study is also available in the Mendeley Data respository in the folder "Neural Network Machine Learning."

Received: 27 February 2024; Accepted: 8 April 2025;
Published online: 18 April 2025

References

1. Biot, M. A. General theory of Three-Dimensional consolidation. *J. Appl. Phys.* **12**, 155–164 (1941).
2. Korbel, A., Embury, J. D., Hatherly, M., Martin, P. L. & Erbsloh, H. W. Microstructural aspects of strain localization in Al Mg alloys. *Acta Metall.* **34**, 1999–2009 (1986).
3. Paesold, M., Bassom, A., Regenauer-Lieb, K. & Veveakis, M. Conditions for the localisation of plastic deformation in temperature sensitive viscoplastic materials. *J. Mech. Mater. Struct.* **11**, 113–136 (2016).
4. Papanicolopulos, S.-A. & Veveakis, E. Sliding and rolling dissipation in cosserat plasticity. *Granul. Matter* **13**, 197–204 (2011).
5. Dewhurst, D. N. & Jones, R. M. Geomechanical, microstructural, and petrophysical evolution in experimentally reactivated cataclasites: Applications to fault seal prediction. *AAPG Bull.* **86**, 1383–1405 (2002).
6. Rattez, H. & Veveakis, M. Weak phases production and heat generation control fault friction during seismic slip. *Nat. Commun.* **11**, 350 (2020).
7. Lesueur, M., Poulet, T. & Veveakis, M. Three-scale multiphysics finite element framework (fe3) modelling fault reactivation. *Computer Methods Appl. Mech. Eng.* **365**, 112988 (2020).
8. Drake, T. G. Granular flow: physical experiments and their implications for microstructural theories. *J. Fluid Mech.* **225**, 121–152 (1991).

9. Rattez, H. et al. Effect of grain size distribution on the shear band thickness evolution in sand. *Géotechnique* **72**, 350–363 (2022).
10. Guével, A., Rattez, H. & Veveakis, E. Morphometric description of strength and degradation in porous media. *Int. J. Solids Struct.* **241**, 111454 (2022).
11. Cui, K. et al. Microstructure, mechanical properties, and reinforcement mechanism of carbide toughened ZrC-based ultra-high temperature ceramics: A review. *Compos. Interfaces* **29**, 729–748 (2022).
12. Zhang, B., Ghimbeu, C. M., Laberty, C., Vix-Guterl, C. & Tarascon, J.-M. Correlation between microstructure and na storage behavior in hard carbon. *Adv. Energy Mater.* **6**, 1501588 (2016).
13. Augat, P. & Schorlemmer, S. The role of cortical bone and its microstructure in bone strength. *Age Ageing* **35**, ii27–ii31 (2006).
14. Homer, E. R. High-throughput simulations for insight into grain boundary structure-property relationships and other complex microstructural phenomena. *Comput. Mater. Sci.* **161**, 244–254 (2019).
15. De Carlo, F. et al. TomoBank: a tomographic data repository for computational x-ray science. *Meas. Sci. Technol.* **29**, 034004 (2018).
16. Aboulhassan, A., Hadwiger, M. & Wodo, O. Extracting topology, shape and size from heterogenous microstructure. *Comput. Mater. Sci.* **173**, 109402 (2020).
17. Naderi, S., Heath, J. P. & Dean, J. S. Morphology characterisation of inclusions to predict the breakdown strength in electro-ceramic materials: Microstructure modelling. *Ceram. Int.* **45**, 361–368 (2019).
18. Wang, Z. Contour feature identification of metal microstructures. *Results Mater.* **6**, 100092 (2020).
19. Campbell, A. et al. Automated analysis of platelet microstructures using a feature length orientation space. *J. Mater. Sci.* **57**, 1448–1461 (2022).
20. Campbell, A., Murray, P., Yakushina, E., Marshall, S. & Ion, W. New methods for automatic quantification of microstructural features using digital image processing. *Mater. Des.* **141**, 395–406 (2018).
21. Armstrong, R. T. et al. Porous media characterization using minkowski functionals: Theories, applications and future directions. *Transp. Porous Media* **130**, 305–335 (2019).
22. Hikage, C. et al. Minkowski functionals of SDSS galaxies I: Analysis of excursion sets. *Publ. Astron Soc. Jpn Nihon Tenmon Gakkai* **55**, 911–931 (2003).
23. Slotte, P. A., Berg, C. F. & Khanamiri, H. H. Predicting resistivity and permeability of porous media using minkowski functionals. *Transp. Porous Media* **131**, 705–722 (2020).
24. Klain, D. A. A short proof of hadwiger's characterization theorem. *Mathematika* **42**, 329–339 (1995).
25. Rattez, H., Stefanou, I., Sulem, J., Veveakis, M. & Poulet, T. The importance of Thermo-Hydro-Mechanical couplings and microstructure to strain localization in 3D continua with application to seismic faults. part II: Numerical implementation and post-bifurcation analysis. *J. Mech. Phys. Solids* **115**, 1–29 (2018).
26. Mosser, L., Dubrule, O. & Blunt, M. J. Reconstruction of three-dimensional porous media using generative adversarial neural networks. *Phys. Rev. E* **96**, 043309 (2017).
27. Scholz, C. et al. Direct relations between morphology and transport in boolean models. *Phys. Rev. E Stat. Nonlin. Soft Matter Phys.* **92**, 043023 (2015).
28. Aoyagi, T. High-throughput prediction of stress-strain curves of thermoplastic elastomer model block copolymers by combining hierarchical simulation and deep learning. *MRS Adv.* **6**, 32–36 (2021).
29. Yang, C., Kim, Y., Ryu, S. & Gu, G. X. Prediction of composite microstructure stress-strain curves using convolutional neural networks. *Mater. Design.* **189**, 108509 (2020).
30. Yu, C. H., Qin, Z. & Buehler, M. J. Artificial intelligence design algorithm for nanocomposites optimized for shear crack resistance. *Nano Futures* **3**, 035001 (2019).
31. Gu, G. X., Chen, C. T., Richmond, D. J. & Buehler, M. J. Bioinspired hierarchical composite design using machine learning: Simulation, additive manufacturing, and experiment. *Mater. Horiz.* **5**, 939–945 (2018).
32. Gu, G. X., Chen, C. T. & Buehler, M. J. De novo composite design based on machine learning algorithm. *Extrem. Mech. Lett.* **18**, 19–28 (2018).
33. Prodanovic, M., Esteva, M. & Hanlon, M. Digital rocks portal. https://www.digitalrocksportal.org/ (2015). Accessed: 2023-5-30.
34. Lie, K.-A. & Mallison, B. T. Mathematical models for oil reservoir simulation. In Engquist, B. (ed.) *Encyclopedia of Applied and Computational Mathematics*, 850–856 (Springer Berlin Heidelberg, Berlin, Heidelberg, 2015).
35. Pore-based architecture and representative element volume evaluation in artificial sand packs and natural rock cores in various fields of science and industrial applications. *Pet. Sci*.**19**, 1473–1482 (2022).
36. Costanza-Robinson, M. S., Estabrook, B. D. & Fouhey, D. F. Representative elementary volume estimation for porosity, moisture saturation, and air-water interfacial areas in unsaturated porous media: Data quality implications. *Water Resour. Res*. **47**, https://doi.org/10.1029/2010WR009655 (2011).
37. Legland, D., Arganda-Carreras, I. & Andrey, P. MorphoLibJ: integrated library and plugins for mathematical morphology with ImageJ. *Bioinformatics* **32**, 3532–3534 (2016).
38. Meyer, F. & Beucher, S. Morphological segmentation. *J. Vis. Commun. Image Represent.* **1**, 21–46 (1990).
39. Serra, J.*Image Analysis and Mathematical Morphology* (Academic Press, Inc., USA, 1983).
40. Lindsay, A. D. et al. 2.0 - MOOSE: Enabling massively parallel multiphysics simulation. *SoftwareX* **20**, 101202 (2022).
41. Poulet, T. & Veveakis, M. A viscoplastic approach for pore collapse in saturated soft rocks using REDBACK: An open-source parallel simulator for rock mechanics with dissipative feedBACKs. *Comput. Geotech.* **74**, 211–221 (2016).
42. Lesueur, M., Casadiego, M. C., Veveakis, M. & Poulet, T. Modelling fluid-microstructure interaction on elasto-visco-plastic digital rocks. *Geomech. Energy Environ.* **12**, 1–13 (2017).
43. Adhikary, D. P., Jayasundara, C., Podgorney, R. K. & Wilkins, A. H. A robust return-map algorithm for general multisurface plasticity. *Int. J. Numer. Methods Eng.* **109**, 218–234 (2016).
44. Frankel, A. L., Jones, R. E., Alleman, C. & Templeton, J. A. Predicting the mechanical response of oligocrystals with deep learning. *Comput. Mater. Sci.* **169**, 109099 (2019).
45. Hassanin, H., Alkendi, Y., Elsayed, M., Essa, K. & Zweiri, Y. Controlling the properties of additively manufactured cellular structures using machine learning approaches. *Adv. Eng. Mater.* **22**, 1901338 (2020).
46. Liang, L., Liu, M., Martin, C. & Sun, W. A deep learning approach to estimate stress distribution: a fast and accurate surrogate of finite-element analysis. *J. Roy. Soc. Interf.* **15**, 20170844 (2018).
47. Salmenjoki, H., Alava, M. J. & Laurson, L. Machine learning plastic deformation of crystals. *Nat. Commun.* **9**, 5307 (2018).
48. Yang, Z., Yu, C.-H. & Buehler, M. J. Deep learning model to predict complex stress and strain fields in hierarchical composites (2021).
49. Peloquin, J. & Lindqwister, W. Neural network architecture and training data for prediction of porous material mechanical properties based on their microstructure. https://data.mendeley.com/datasets/9wpm748fb3/3 (2024).

Acknowledgements

We wish to acknowledge the support of the U.S. National Science Foundation via research funding from National Science Foundation Project CMMI-2042325 as well as the Duke Artificial Intelligence and Material Science (AIM) Traineeship Program under National Science Foundation grant DGE-2022040.

Author contributions

All authors jointly planned and designed the research. W.L. and J.P. led research efforts and are considered co-first authors. W.L. and J.P. wrote the original draft, and all authors contributed substantially to revisions. W.L. conceptualized the usage of Minkowski functionals and developed the FEA code needed for this project. J.P. took the lead on 3D printing of samples, and also developed the machine learning model used in the study. L.D. provided a significant amount of the total microstructural CT data. K.G. and M.V. provided laboratory resources and guidance.

Competing interests

The authors declare no competing interests.

Additional information

Supplementary information The online version contains supplementary material available at https://doi.org/10.1038/s44172-025-00410-9.

Correspondence and requests for materials should be addressed to W. Lindqwister or J. Peloquin.

Peer review information *Communications Engineering* thanks the anonymous reviewers for their contribution to the peer review of this work. Primary Handling Editors: [Emanuela Bosco] and [Miranda Vinay]. Peer reviewer reports are available.